Materials Today Communications 46 (2025) 112598

Contents lists available at ScienceDirect

Materials Today Communications

journal homepage: www.elsevier.com/locate/mtcomm

Evaluation of the photothermal performance of the Prussian blue/hydroxyapatite composite

Achilley Nahid Barros Costa [a], Josilene Lima Serra [a], Israel da Luz Rodrigues [a], Leonardo Tadeu Boaes Mendonça [b], Goreti Pereira [c], Elisabete M.S. Castanheira [d], Samuel Filgueira Rodrigues [a], Antônio E.M. Paiva [a], Sérgio R.S. Veloso [d,e], Ana Rita O. Rodrigues [d], Gricirene Sousa Correia [a,*]

[a] Federal Institute of Education, Science and Technology of the State of Maranhão, São Luis, Maranhão, Brazil
[b] Department of Chemical Technology, Federal University of Maranhão, São Luis, Maranhão, Brazil
[c] Department of Chemistry and CESAM, University of Aveiro, Aveiro, Portugal
[d] Physics Centre of Minho and Porto Universities (CF-UM-UP), University of Minho, Braga 4710-057, Portugal
[e] CINBIO, Universidad de Vigo, Vigo, Spain

ARTICLE INFO

Keywords:
Prussian blue
Calcium phosphate
Alginate
Photothermal

ABSTRACT

In this study, Prussian Blue (PB) and hydroxyapatite (HAp) composites were developed and synthesized in situ within an alginate gel, resulting in materials with excellent photothermal conversion efficiency. Structural information and morphology of the composites were obtained by using X-ray diffraction (XRD), Fourier-transform infrared spectroscopy (FTIR), UV–vis absorption spectroscopy, and Scanning Elcetron Microscopy (SEM) and Transmission Electron Microscopy (TEM) techniques. Photothermal performance was evaluated under near-infrared (NIR) radiation at 808 nm. The micrographs showed the characteristic cubic morphology of PB as well as its encapsulation by hydroxyapatite phase during synthesis. The UV–vis absorption spectroscopy shows an increase in the absorption band in the region around 800 nm for the composite due to the presence of Prussian blue. XRD analysis revealed the presence of PB and HAp phases in the composite with 2 % of alginate. Photothermal tests showed that a composite containing 2 % alginate promoted excellent temperature increase and stability, achieving a ΔT of approximately 23°C while maintaining comparable efficacy to pure PB. The composites demonstrated excellent photothermal stability during repeated cycles, suggesting their suitability as photothermal agents. The incorporation of HAp and the presence of alginate did not affect the photothermal behavior of the composites, highlighting their promise potential for the development of future photothermal devices.

1. Introduction

Photothermal therapy (PTT) is an emerging technique where many materials have the ability to absorb infrared and convert it into heat with high efficiency [1].The use of near-infrared (NIR) radiation in PTT serves as excitation source to photothermal agents with targeted absorption to be used in specific areas such as biomedicine, sensing, steam generation and photocatalysis [2]. In this context, photothermal therapy has attracted great interest due to its precise targeting capability, minimal invasiveness, high efficacy, and low side effects [3]. There are many compounds and materials that can exhibit photothermal behaviour including metal nanomaterials [1,2,4], carbon nanomaterials [5,6], and nanocomposites [7], are widely investigated for cancer PTT. Despite the immense research on nanosized PTAs, it is important to develop new materials with the therapeutic effects of both PTT and combination therapies.

Prussian blue appears as a candidate for photothermal therapy with great versatility due to its proven safety, as it is used as a therapeutic substance for detoxifying people contaminated with Cs137 and high biocompatibility. In addition, it has a low cost to obtain, unlike metallic nanoparticles, whose reagents are expensive and difficult to acquire [8–10]. PB, or iron III hexacyanoferrate is characterized by a three-dimensional network of bonds between iron ions in the forms Fe^{2+} and Fe^{3+}, connected by cyanide groups (CN^-) [11]. Its molecular

* Corresponding author.
E-mail address: gricirene.correia@ifma.edu.br (G.S. Correia).

https://doi.org/10.1016/j.mtcomm.2025.112598
Received 2 January 2025; Received in revised form 17 March 2025; Accepted 19 April 2025
Available online 21 April 2025
2352-4928/© 2025 Published by Elsevier Ltd.

formula, $Fe_4^{III}[Fe^{II}(CN)_6]_3$, presents interesting characteristics from a structural point of view. The 4:3 ratio between $Fe^{(III)}$ and $[Fe^{II}(CN)^6]^{4-}$ generates an uneven distribution of the complex ion $[Fe^{II}(CN)_6]^{4-}$, which translates into empty spaces within the PB crystal structure [12]. These randomly generated vacancies allow the insertion of ions or molecules with size approximately equal or smaller than total volume of a single vacancy. This characteristic makes it particularly interesting in biomedical applications, such as delivery systems for pharmacological agents, among other biomedical and technological applications [13]. In addition, it serves as a marker in toxicity studies, where it facilitates the visualization and tracking of substances within biological systems [14]. PB can absorb light in the NIR region, especially around 650–900 nm, an absorption range considered essential for photothermal applications [15]. When irradiated with NIR light, PB converts light energy into heat through charge transfer process between Fe(II) and Fe(III) ions, using cyanide bonds as an energy transfer bridge, resulting in an increase in absorption intensity [16]. This temperature increase can be carefully controlled and used to induce drug release in a localized and selective manner [14,17].

Recently, various strategies have been explored to combine photothermal agents with bioceramic materials [18]. However, developing composite materials with good thermal efficiency remains a significant challenge. Synthetic hydroxyapatite (HAp, $Ca_5(PO_4)_3(OH)$) is a calcium phosphate that mimics the constituents of bone tissue, featuring a hexagonal crystalline structure and a stoichiometric calcium/phosphorus (Ca/P) molar ratio of 1.67 [19,20]. It is widely recognized for its high biocompatibility and bioactivity, facilitating favorable interactions with other ions [11,21]. Although HAp exhibits limitations in photothermal conversion efficiency, its nanoscale synthesis can enhance interaction and stability with photothermal agents.

The *in situ* synthesis of HAp within the alginate gel ensures control over the size of the inorganic crystals [22]. Sodium alginate is well known for its high biocompatibility and biodegradability, consisting of guluronic acid (G) and mannuronic acid (M) regions. The conformation of guluronic acid enables strong coordination of COO^- and OH^- groups with Ca^{2+} ions, leading to the formation of the "egg-box" structure [23,24] The incorporation of HAp nanocrystals with PB into the alginate matrix can modulate the involved components, optimizing their properties. Previous studies investigating the combination of HAp with photothermal agents, such as carbon quantum dots [25] and polydopamine [26] reported low photothermal efficiency, 62.4 % and 12.2 %, respectively, compared to the results obtained in this research.

Here in this investigation, PB was encapsulated into HAp during its synthesis within the alginate gel. The crystalline structure and morphology of the composites were analyzed, focusing on the efficiency and stability of the photothermal response under NIR light irradiation. For the composite under investigation, it was also essential to study the influence of alginate content on photothermal behavior. The results demonstrate the potential of this material for future biomedical and technological applications, innovatively highlighting its unique and promising properties.

2. Methodology

2.1. Reagents

The utilized reagents without purification in this research were: Polyvinylpyrrolidone (PVP, $M_w = 4 \times 10^4$ g.mol^{-1}, Synth brand, 99 % purity), calcium nitrate ($Ca(NO_3)_2{\cdot}4H_2O$, Synth brand, 98,99 % purity), sodium hydrogen phosphate dihydrate ($Na_2HPO_4{\cdot}2H_2O$, Exodo brand, 99 % purity), sodium alginate ($(C_6H_7NaO_6)_n$ Exodo, 98 % purity), hydrochloric acid (HCl, Dinâmica brand, 36,5 % purity), Ethanol (C_2H_6O, Vetec brand, 99,5 %) and sodium hydroxide (NaOH, Dinâmica brand, 98 % purity).

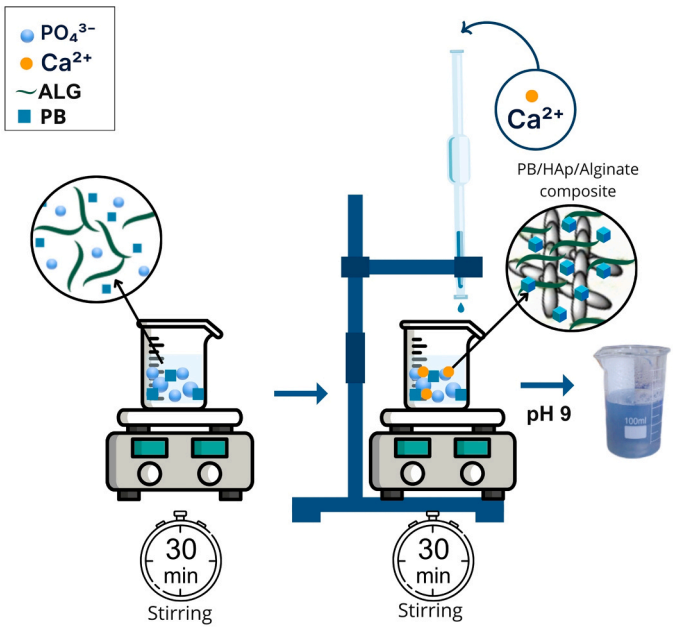


Fig. 1. Synthesis of the Prussian blue and hydroxyapatite composite *in situ* in alginate gel.

2.2. Synthesis of Prussian blue (PB) precipitates

PB crystals were produced by aqueous precipitation using an iron source. To do this, 8 mmol of $Na_4Fe(CN)_6{\cdot}10H_2O$, 2.0 g of PVP, and 4 mL of 0.5 M HCl were added to 400 mL of deionized water and mixed with constant stirring for 30 minutes until it acquired a yellowish colour. The solution was then submitted to a reflux system at 60 °C for 6 hours and left to age for 24 hours. The resulting precipitate was then centrifuged, washed several times with deionized water and ethanol, and finally dried in an oven at 100 °C for 24 hours.

2.3. Preparation of the Prussian blue and hydroxyapatite composite

The composite was prepared using the *in situ* coprecipitation method in the alginate gel, see Fig. 1, following and adapting the procedures proposed by Correia et al. [27]. Next, the reagents $Ca(NO_3)_2{\cdot}4H_2O$ and $Na_2HPO_4{\cdot}2H_2O$ were weighed in such a way that the molar ratio leads to the formation of hydroxyapatite. Composites were prepared with two concentrations (2 and 3 % w/v) of alginate to assess its influence. Sodium alginate was added to 30 mL of 0.01 mol.L^{-1} solution of $Na_2HPO_4{\cdot}2H_2O$ and stirred continuously until it formed a gel. After this, 0.01 g of PB powder was added and stirred for 30 min for complete homogenization.

Subsequently, 30 mL of $Ca(NO_3)_2.4H_2O$ solution containing 0.48 mmol was added by dripping slowly. The pH of the mixture was adjusted to ~9 by adding NaOH solution (2.0 mol.L^{-1}) slowly. After adding all the reagents, the system was stirred for another 30 min at room temperature to complete the reaction and the composite precipitated. The sample was centrifuged and washed several times with distilled water to eliminate residual reagent and dried at 60 °C for 24 h. For comparison purposes, composites without alginate were also prepared, following the same procedure as in the previous section.

For comparison purposes, HAp was synthesized by wet precipitation following the methodology described by Mobasherpour et al. [28]. The precipitate was obtained by the slow and controlled addition of 0.02 mol of $Na_2HPO_4{\cdot}2H_2O$ (Exodo, 99 %) under continuous stirring into an aqueous solution containing 0.04 mol of $Ca(NO_3)_2{\cdot}4H_2O$ (Synth, 98.98 % purity). Subsequently, a NaOH solution (2 mol.L^{-1}, Dinâmica, 98 %) was added until the pH reached 9. The system was kept under

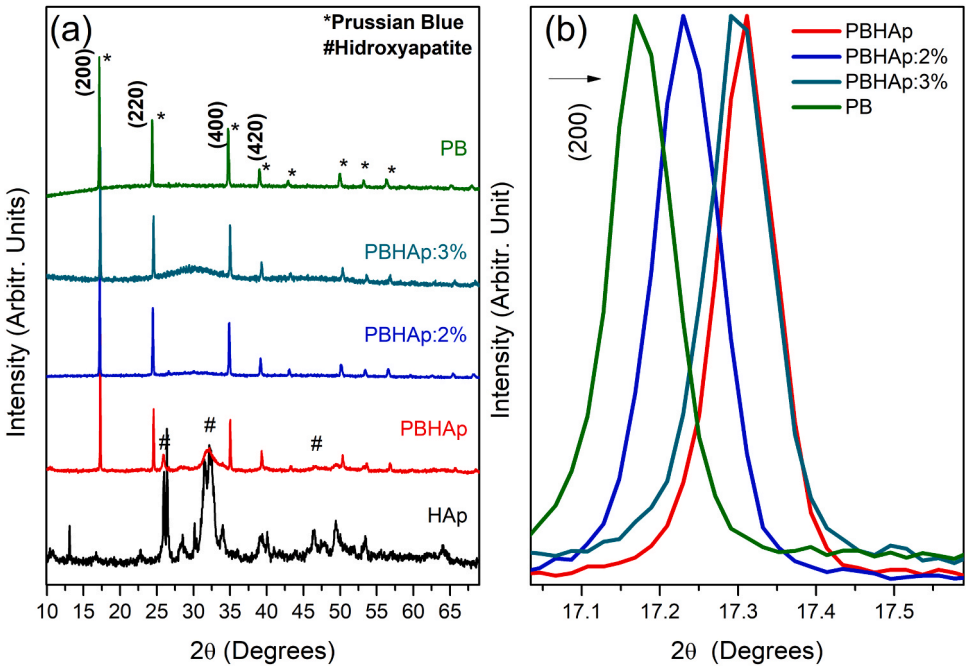


Fig. 2. XRD patterns of samples of (a) Prussian blue (PB), Prussian blue/hydroxyapatite composite without alginate (PBHAp) and with alginate (PBHAp:2 % and PBHAp:3 %) and (b) enlargement (200) peak displacement.

constant stirring for 1 h and then left undisturbed for 24 h to allow complete crystallization. After this period, the precipitates were centrifuged and washed multiple times with distilled water, with a final wash using 99.5 % ethanol solution (Vetec, PA). The material was then dried at 60°C for 24 h, ground using a mortar and pestle, and sieved through a 500 #mesh screen (≤25 μm opening) to prevent agglomeration.

2.4. Characterization and photothermal tests

For the X-ray diffraction (XRD) analysis, a Bruker D8 Advance diffractometer was used, operating with Cu K_α radiation (λ = 1.5418 Å) at 40 kV and 40 mA, equipped with a LynxEye linear detector. The data was collected in Bragg-Brentano geometry, covering the range from 10 to 60º, with a scan rate of 5º/min. Fourier transform infrared (FTIR) characterization was conducted using a Shimadzu IR-Prestige-21 spectrophotometer covering the 400–4000 cm^{-1} range, with a scanning step of 0.1 cm^{-1} and a resolution of 4 cm^{-1}, using KBr pellets. The morphology and microstructure of the samples were examined using scanning electron microscopy (SEM) with a FEI Nova 200 Nano SEM (FEG/SEM), operating at 10–30 kV. Transmission electron microscopy (TEM) was made using a MET-AR JEM-2100, Jeol, Tokyo, Japan, equipped with EDS, Thermo Scientific. For the UV/vis/NIR absorption, a Shimadzu UV-3600 Plus UV/Vis/NIR spectrophotometer was used.

In the photothermal assays, aqueous dispersions of each sample were prepared in phosphate-buffered saline (PBS) at a concentration of 1 mg/mL. The samples were irradiated with a λ = 808 nm laser in the NIR with a power of 1.0 W/cm^2 at ambient pressure, and the temperature variations were measured with a T type thermocouple connected to a digital multimeter (Agilent U1242A). In each heating and cooling cycle, the dispersion was irradiated with a power of 1.0 W/cm^2 for 20 minutes (laser on) and then maintained for 20 minutes (laser off) and the initial room temperature was 23°C, ambient pressure and 65 % humidity. For comparison purposes, measurements were taken only with water under the same conditions. The efficiency was calculated using the photothermal conversion formula [29], given as follows in Eq. 1:

$$\eta = \frac{hS(T_{max} - T_{surr}) - Q_{dis}}{I(1 - 10^{-A_{808}})} \quad (1)$$

In the Eq. 1, η represents the photothermal conversion efficiency; h is the heat transfer coefficient; **S** is the surface area of the sample; T_{max} and T_{surr} are the maximum and ambient temperatures, respectively; Q_{dis} is the dissipated energy; I is the incident laser power; and A_{808} is the absorbance of the sample at 808 nm.

3. Results and discussion

3.1. X-ray diffraction

The diffractograms of PB, composite without alginate (PBHAp), and with alginate (PBHAp:2 % and PBHAp:3 %) are shown in Fig. 2. In all samples, it is possible to observe the presence of the cubic phase of PB, configuring the formation of a face center cubic crystalline structure belonging to the Fm-3m space group. The peak reflections of the HAp phase were observed at 25.6°, 26.62°, and 31.9° (# JCPDS 9–2216) in the PBHAp composite pattern [30]. The appearance of these small peaks in PBHAp indicates that the crystalline structures of HAp and PB remained stable until reaching the final pH adjustment of 9 during the synthesis.

In the case of composites containing alginate, the peaks are less intense. It is suggested that this is due to *in situ* nucleation which induces the formation of nanometric crystals of the hydroxyapatite phase. It can also be observed that in the PBHAp:3 % sample, the 53.4º peak shows the cubic phases of PB and HAp overlapping, confirming the presence of both phases in the composite structure [31–33]. Therefore, the diffractograms of the composites reveal the coexistence of the Prussian blue and hydroxyapatite phases, showing a highly crystalline structure (sharp peaks, no broadening of the baseline) for the PB phase and low crystallinity in the HAp, especially in the samples containing alginate.

It is possible to observe the shift of the peak corresponding to the (200) plane for high angle. This effect is possibly due to the presence of hydroxyapatite in large quantities in the composite or to the sodium alginate distorting the structure of the Prussian blue. To calculate the crystallite size, the Scherrer equation was used, considering the most

Table 1
Structural parameters from samples and crystalite size.

	FWHM	Position	Radiation (CuKα, Å)	K	$D_{Scherrer}$ (nm)
PB	0.10092	17.1760	1.5406	0.94	83.15
PBHap	0.09189	17.3099	1.5406	0.94	91.34
PBHap:2 %	0.10577	17.2339	1.5406	0.94	79.34
PBHap:3 %	0.10133	17.3009	1.5406	0.94	82.83

intense peak.

$$D = \frac{K\lambda}{\beta \cos\theta}$$

Where K is the shape factor, 0.94, β is the measured broadening minus the instrumental broadening, and lambda is the Kα radiation emission of copper. Observing Table 1, it is possible to observe that the samples present not only an increase in width at half height but also a displacement of the (002) peak, which generally resulted in a decrease in the crystallite size due to the combination of sodium alginate and hydroxyapatite with Prussian blue.

3.2. UV/Vis/NIR absorption and fourier transform infrared (FTIR) spectroscopies

The UV/Vis/NIR absorption and FTIR spectra of PB and Prussian blue/hydroxyapatite composites are shown in Fig. 3. It can be seen in Fig. 3(a), the characteristic bands of the isolated phases. The Prussian blue band around 800 nm is present, which corresponds to the charge transfer process between Fe^{2+} and Fe^{3+} and is responsible for generating the charge carriers that will diffuse through the lattice, leading to the photothermal effect [34]. This band is present in all composites but with greater intensity in the PBHAp:2 % sample.

The Fig. 3(b) shows the FTIR spectra of PB, Prussian blue/hydroxyapatite composites and hydroxyapatite (HAp). In all the samples, the characteristic vibrational modes of PB are evident in the bands at 2389 cm^{-1} , which correspond to the stretching of the C≡N bond, 2299 and 2075 cm^{-1} are specifically associated with the Fe^{2+}-C≡N-Fe^{3+} bond, 1385 and 1630 cm^{-1} are attributed to the carbonyl group O═C-O and C═O, respectively, resulting from oxygen-containing functional groups [35,36]. It is worth noting that in the PBHAp sample, which does not contain alginate, the bands at 601 and 495 cm^{-1} , related to the iron-cyanide complex (Fe-C≡N), were not detected. This is probably due to the high vibrational intensity of the phosphate group (PO_4^{3-}) belonging to hydroxyapatite (HAp), which, in this sample, is not involved in the alginate matrix. The absence of alginate may allow the phosphate group to exhibit a more intense vibration, suppressing the bands associated with the iron-cyanide complex. Phosphate groups (PO_4^{3-}) were also observed at 1035 cm^{-1} in the samples PBHAp:3 %, PBHAp:2 %, and PBHAp (sample without alginate), confirming the presence of HAp in the composite, and the 1425 cm^{-1} band refers to the C-H bending vibration, which may be associated with the presence of the alginate polymer in these composites [37]. This information corroborates the presence of hydroxyapatite in the composite as well as in the x-ray diffraction patterns.

3.3. Scanning electron microscopy (SEM) images and elemental mapping analysis

The Fig. 4 shows the morphology of PB (Fig. 4(a)), PBHAp (Fig. 4 (b)), PBHAp:2 % (Fig. 4(c)), and PBHAp:3 % (Fig. 4(d)). In Fig. 4(a), cubic crystals with rough surfaces were observed, with an average size of 1.2 ± 0.8 μm. As for the PBHAp sample, it was possible to see numerous agglomerated particles in the shape of thin plates (Fig. 4(b)), characteristic of the morphology of HAp [38]. The Figs. 4(c) and 4(d) show a dense aggregation of the composites, likely resulting from the *in situ* nucleation of HAp within the alginate polymer chain [39]. However, due to the lower alginate concentration, the PBHAp:2 % sample exhibited more dispersed clusters. These characteristics may have been influenced by the presence of alginate, due to electrostatic interactions and hydrogen bonds between PB, alginate[40] and HAp [41]. The images show that the characteristic morphology of Prussian blue disappears as a result of the synthesis of hydroxyapatite, which could lead to the conclusion that the compound has dissolved. However, the XRD and infrared results show that Prussian blue is still present, possibly surrounded by hydroxyapatite. Fig. 4(e), (f), and (g) show the elemental mapping images of the PBHAp, PBHAp:2 % and PBHAp:3 % samples, respectively. There is a clear distribution of the constituent elements of

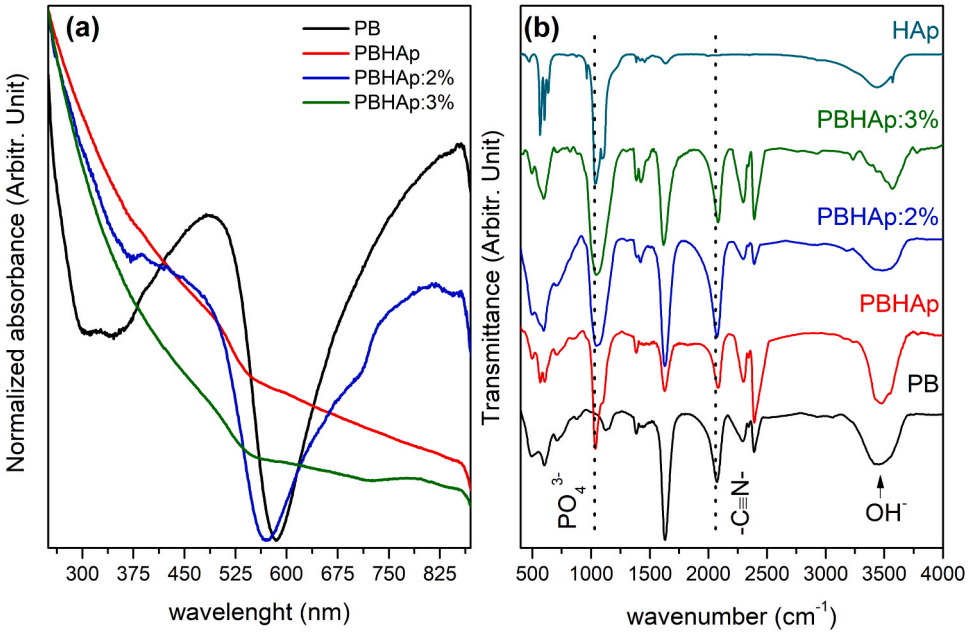


Fig. 3. (a) UV/Vis/NIR absorption spectra and (b) FTIR spectra with principal vibrational modes of Prussian blue (PB), Prussian blue/hydroxyapatite composites and hydroxyapatite (HAp).

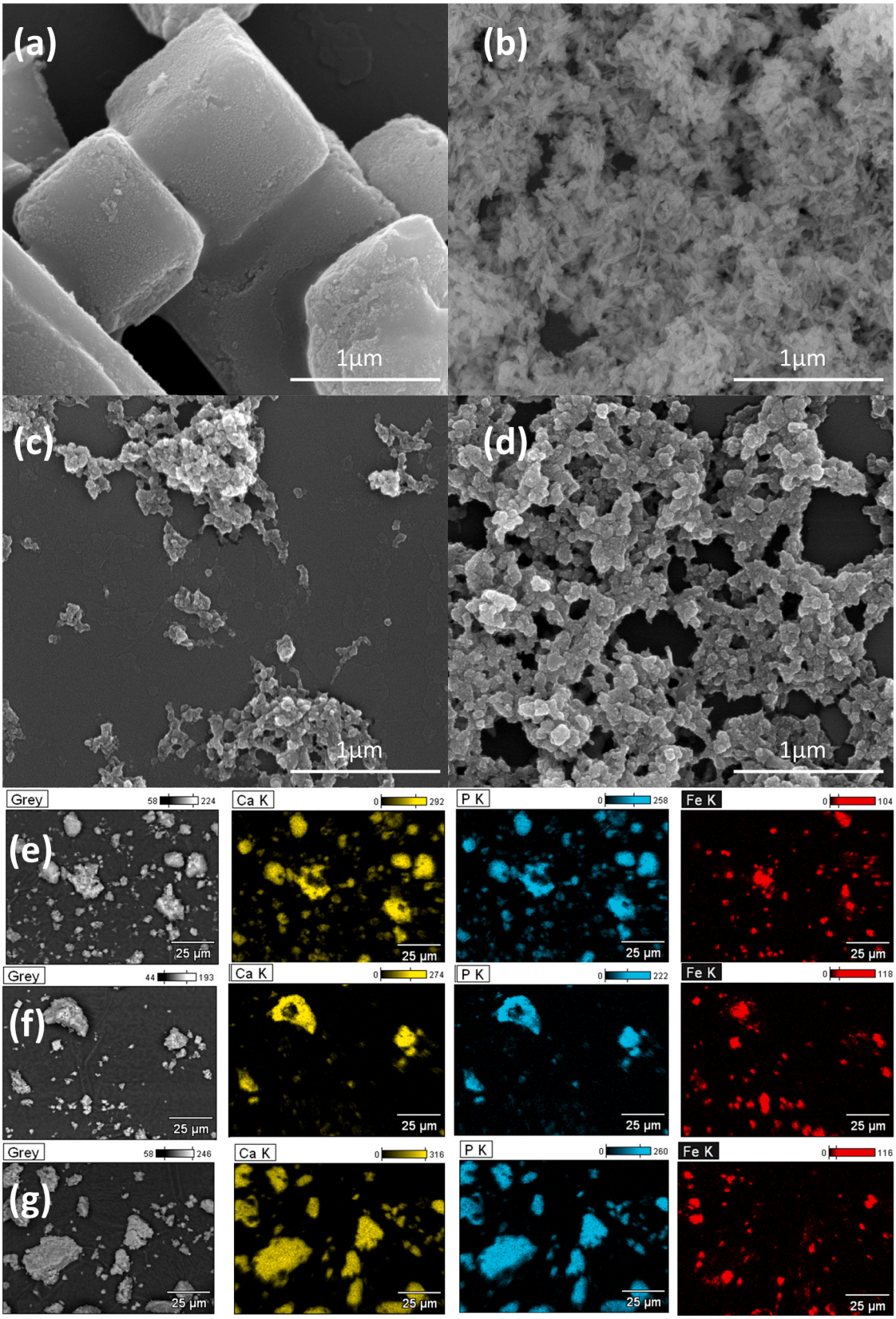


Fig. 4. Scanning electron microscopy of the samples at 100 kx magnification (a) PB, (b) PBHAp, (c) PBHAp:2 %, (d) PBHAp:3 %, and (e-g) their elemental image mapping.

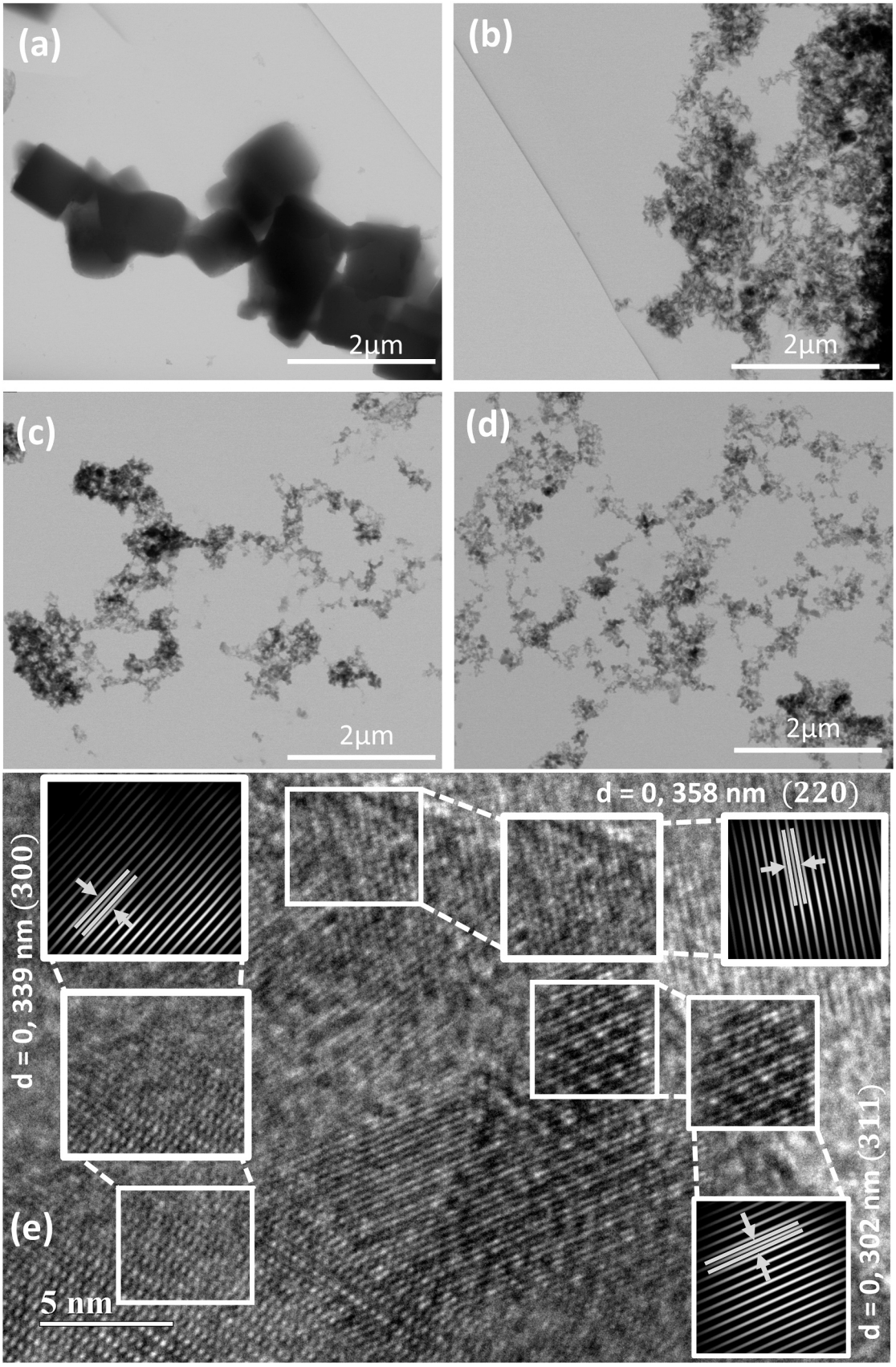


Fig. 5. Transmission Electron Microscopy images of (a) PB, (b) PBHAp, (c) PBHAp:2 % and (d) PBHAp:3 % at 50kx magnification, and (e) HR-TEM image.

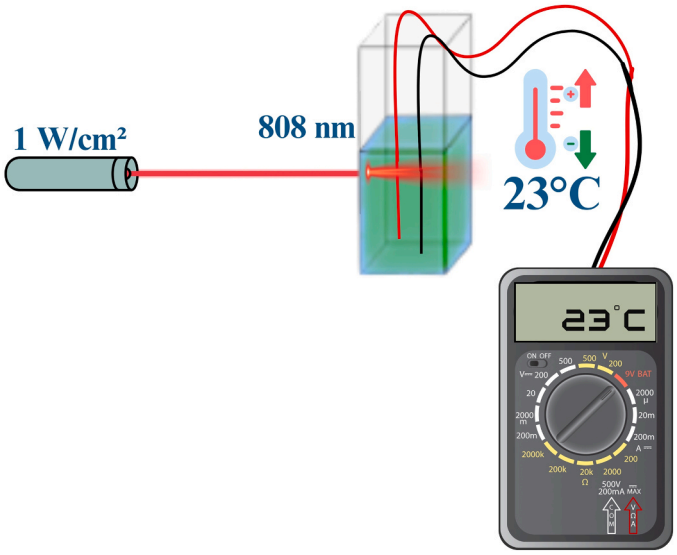


Fig. 6. Schematic representation of the set up to photothermal experiment: a NIR laser (808 nm wavelength and 1 W/cm²) was used to irradiate the solution containing the samples, while the temperature is measured in real time by a thermocouple.

PB (Fe) and HAp (Ca and P) and confirms that Prussian blue is surrounded by hydroxyapatite.

3.4. Transmission electron microscopy (TEM) and high-resolution TEM (HR-TEM)

The TEM images are displayed in Fig. 5. Fig. 5(a) confirms the morphology of cubic PB crystals of micrometric size surrounded by clusters of nanometric crystals. Fig. 5(b), corresponding to PBHAp, shows numerous needle-shaped nanometric crystals, indicative of HAp [42] and identified by XRD (Fig. 2). This is probably due to the *in situ* synthesis of the HAp in the alginate gel, which results in the formation of nanocrystals, as described elsewhere [43]. Other crystals with a different, unclear morphology are present in this image and that may be due to PB nanocubes. As shown in Figs. 5(c) and 5(d) the precipitates are embedded within the alginate matrix. The sample with the lowest alginate content (Fig. 5(c)) shows a higher concentration of PB crystals. Thus, it can be confirmed that this method of preparing the composite preserved the cubic morphology of the PB, allowing this material to contribute to the photothermal effect.

HR-TEM image of the same sample (PBHAp:2 %), with software analysis reveal lattice spacings of 0.339, 0.358, and 0.302 nm, as shown in Fig. 5(e). These values correspond to the (3 0 0), (2 2 0), and (3 1 1) planes of the cubic PB particles, respectively, aligning with the XRD results (ICSD-001277) where high crystallinity of the phase is observed. The transmission images agree with the scanning electron microscopy images, where the morphologies undergo strong changes as hydroxyapatite is incorporated.

3.5. Photothermal tests

For photothermal analysis, an experimental setup was used, as illustrated in Fig. 6. This setup allowed a rigorous evaluation of the photothermal efficiency over each sample under controlled irradiation conditions.

It is known that Prussian blue has a high infrared absorption capacity due to the presence of Fe2 + and Fe3 + ions linked by the C═N group, allowing a charge transfer during excitation. When the excited electrons return to the ground state, they tend to decay non-radiatively, causing a

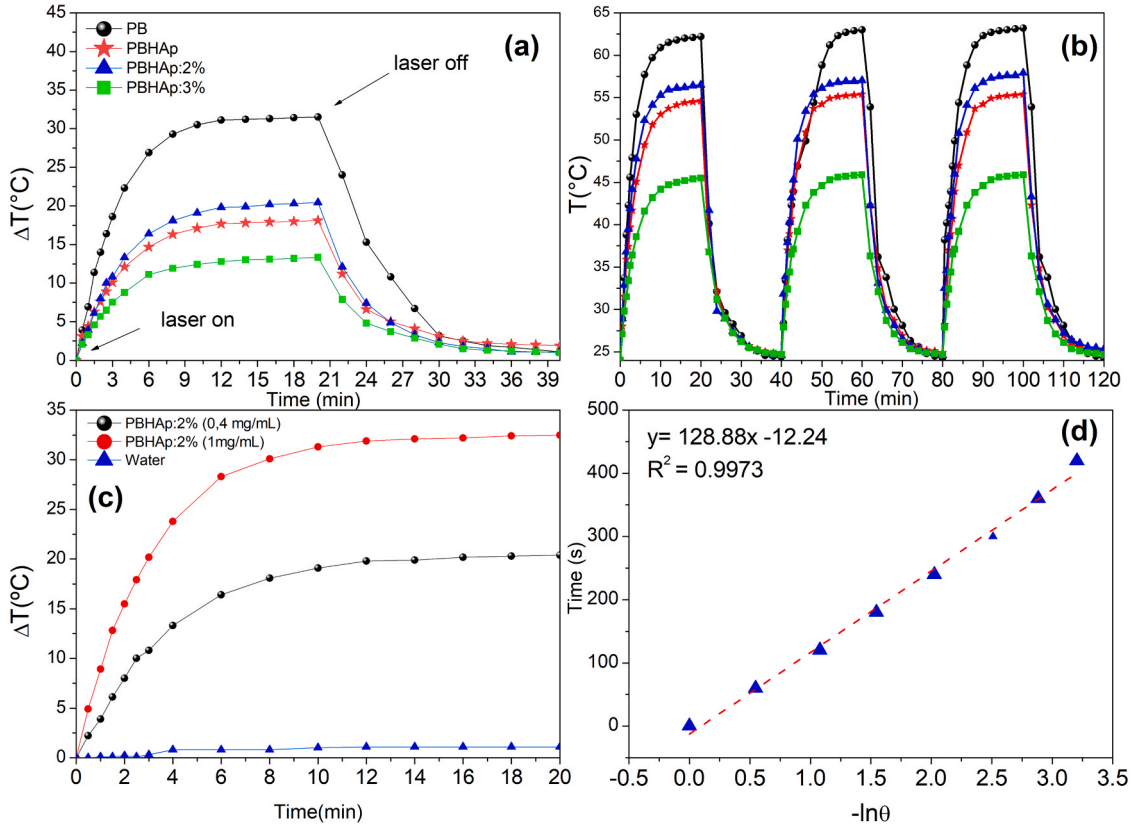


Fig. 7. (a) Comparison of each sample in the photothermal test (0.4 mg.L^{-1}) (b) Heating-cooling cycles (c) tests with different concentrations of PBHAp:2 % and (d) conversion factor efficiency. The samples were irradiated with an 808 nm laser (1 W/cm²).

local temperature increase. This phenomenon gives rise to the photothermal behavior of Prussian blue [44]. The Fig. 7(a) and (b) show the results of photothermal measurement using a near-infrared laser (λ = 808 nm, 1 W/cm^2) of the PB and PBHAp samples, with and without alginate, as well as the photostability in three irradiation cycles, where the initial temperature was maintained at 23 °C. To evaluate the photothermal stability, the samples were subjected to a 20 minute natural cooling cycle (laser off) after 20 minutes of continuous irradiation (laser on). It was observed that the incorporation of 2 % alginate (PBHAp:2 %) did not affect the photothermal performance, reaching a ΔT of approximately 23 °C at a concentration of 0.4 mg/mL after 20 minutes. However, increasing the alginate concentration to 3 % (PBHAp:3 %) resulted in a reduction in the ΔT to approximately 15 °C. This decrease in photoconversion is directly associated with the infrared absorption capacity of samples with a higher alginate content. This behavior is observed in the UV–vis absorption spectrum, which is also supported by the decrease in the intensity of the signal corresponding to the C≡N group in FTIR results, responsible for infrared absorption in the Prussian blue structure [45]. Despite the lower performance, the results remain superior to the values reported in the literature regarding PTAs surrounded by gels, which indicated a maximum ΔT of 12 °C [41].

Furthermore, high concentrations of alginate can increase the opacity of the system, hindering light transmission to the photothermal agents. Simultaneously, a denser matrix promotes greater thermal dissipation, reducing the efficiency of energy conversion into heat. [39].

Moreover, similar photothermal behavior was observed for the PBHAp and PBHAp:2 % samples. Also, in the assays performed over three irradiation cycles, for samples at a concentration of 1.0 mg/mL, the photothermal performance remained consistent, without any significant loss, evidencing excellent photostability. This indicates that alginate concentrations until 2 % can favor or, at least, not compromise the photothermal performance

This result is supported by the photothermal conversion efficiency data, where the PBHAp:2 % sample reached a value close (89 %) to that of the sample containing only PB (90 %). The Fig. 7(c) displays the suspension of particles PBHAp:2 % samples at concentrations of 0.4 and 1.0 mg/mL when exposed to the NIR laser. It can be observed that the temperature variation of pure water was practically negligible. On the other hand, the increase in temperature was proportional to the concentration of suspension attributed to the photothermal effect of the PBHAp:2 % composite. Thus, it can be concluded that all composites demonstrated excellent heat generation capacity and maintained photostability throughout three laser irradiation cycles. This indicates that the obtained composites have great potential to be used as ideal photothermal agents in bone tissue cancer therapy, as they can not only be incorporated into the scaffold but also stimulate osteogenesis and exhibit antitumor effects.

4. Conclusion

In this work, PB and HAp composites were successfully synthesized *in situ* within an alginate gel matrix. X-ray diffraction (XRD) patterns and Fourier-transform infrared spectroscopy (FTIR) confirmed the coexistence of PB and HAp crystals through their respective diffraction peaks and vibrational modes. SEM and TEM microscopic images revealed composites embedded in the alginate matrix, altering their morphologies but maintaining the structural integrity of the Prussian blue and nanocrystals characteristic of HAp. Photothermal performance under NIR laser irradiation showed that composites with 2 % alginate (PBHAp:2 %) achieved a temperature increase (ΔT) of 23 °C, with minimal reduction compared to pure PB. Although the inclusion of 3 % alginate reduced the ΔT to approximately 15°C, this performance still surpassed many polymers matrix-based photothermal agents reported in the literature. Additionally, the temperature variation over time demonstrated consistent photothermal stability across three cycles. Therefore, this study confirms that the composite consisting of PB, HAp, and alginate offers suitable physical stability and photothermal efficiency.

CRediT authorship contribution statement

Correia Gricirene Sousa: Writing – review & editing, Writing – original draft, Visualization, Supervision, Project administration, Conceptualization. **Barros Costa Achilley Nahid:** Resources, Methodology, Investigation, Formal analysis, Data curation, Conceptualization. **Veloso Sérgio R. S.:** Investigation, Formal analysis. **Rodrigues Ana Rita O.:** Supervision, Investigation, Formal analysis. **Boaes Mendonça Leonardo Tadeu:** Writing – original draft, Visualization, Supervision, Methodology. **Pereira Goreti:** Writing – review & editing, Writing – original draft, Supervision. **Serra Josilene Lima:** Visualization, Resources. **da Luz Rodrigues Israel:** Methodology, Investigation. **Castanheira Elisabete M. S.:** Writing – review & editing, Writing – original draft, Investigation, Conceptualization. **Rodrigues Samuel Filgueira:** Visualization, Project administration, Funding acquisition. **Paiva Antônio E. M.:** Supervision, Funding acquisition, Formal analysis.

Declaration of Competing Interest

The authors declare that they have no known competing financial interests or personal relationships that could have appeared to influence the work reported in this paper.

Acknowledgments

This work was supported by the Maranhão Foundation for Research and Scientific and Technological Development (FAPEMA). We would like to thank the contributions of CF-UM-UP (financial support UIDB/04650/2020 by FCT-Portugal), CESAM (financed by FCT/MCTES UIDP/50017/2020+UIDB/50017/2020+LA/P/0094/2020), and the Colloidal Systems Laboratory of the Federal University of Maranhão, which provided space and equipment for the development of the research, and the Multiuser Laboratory of High-Resolution Microscopy of the Federal University of Goiás (LabMic/UFG).

Data Availability

Data will be made available on request.

References

[1] J.-W. Lu, F. Yang, Q.-F. Ke, X.-T. Xie, Y.-P. Guo, Magnetic nanoparticles modified-porous scaffolds for bone regeneration and photothermal therapy against tumors, Nanomedicine 14 (2018) 811–822, https://doi.org/10.1016/j.nano.2017.12.025.
[2] B. Zheng, Z. Han, G. Wu, Y. Liu, C. Liu, F. Ma, Synthesis of near infrared-activatable KxWO3 nanorods for photothermal therapy, Mater. Lett. 212 (2018) 194–197, https://doi.org/10.1016/j.matlet.2017.10.093.
[3] L. Lu, C. Zhang, B. Zou, Y. Wang, Hollow prussian blue nanospheres for photothermal/chemo-synergistic therapy< /p> . Int J. Nanomed. 15 (2020) 5165–5177, https://doi.org/10.2147/IJN.S252505.
[4] J. MacPhee, T. Kinyenye, B.J. MacLean, E. Bertin, G.L. Hallett-Tapley, Investigating the photothermal disinfecting properties of light-activated silver nanoparticles, Ind. Eng. Chem. Res 60 (2021) 17390–17398, https://doi.org/10.1021/acs.iecr.1c03165.
[5] Y.A. Cheon, J.H. Bae, B.G. Chung, Reduced graphene oxide nanosheet for chemo-photothermal therapy, Langmuir 32 (2016) 2731–2736, https://doi.org/10.1021/acs.langmuir.6b00315.
[6] W. Shi, Q. Han, J. Wu, C. Ji, Y. Zhou, S. Li, et al., Synthesis mechanisms, structural models, and photothermal therapy applications of top-down carbon dots from carbon powder, graphite, graphene, and carbon nanotubes, Int J. Mol. Sci. 23 (2022) 1456, https://doi.org/10.3390/ijms23031456.
[7] F. Costa-e-Sá, M. Comís-Tuche, C. Spuch, E.M.S. Castanheira, S.R.S. Veloso, Sequential release of drugs from dual-delivery plasmonic nanogels containing lipid-gated mesoporous silica-coated gold nanorods, J. Drug Deliv. Sci. Technol. 96 (2024) 105723, https://doi.org/10.1016/j.jddst.2024.105723.
[8] W. Gao, Y. Wang, Y. Zheng, X. Cai, Prussian blue nanoparticle: from a photothermal conversion agent and a drug delivery system, to a bioactive drug, Acc. Mater. Res 5 (2024) 687–698, https://doi.org/10.1021/accountsmr.3c00260.

[9] H.A. Hoffman, L. Chakrabarti, M.F. Dumont, A.D. Sandler, R. Fernandes, Prussian blue nanoparticles for laser-induced photothermal therapy of tumors, RSC Adv. 4 (2014) 29729, https://doi.org/10.1039/C4RA05209A.
[10] J. Liao, Y. Li, H. Li, J. Liu, Y. Xie, J. Wang, et al., Preparation, bioactivity and mechanism of nano-hydroxyapatite/sodium alginate/chitosan bone repair material, J. Appl. Biomater. Funct. Mater. 16 (2018) 28–35, https://doi.org/10.5301/jabfm.5000372.
[11] W.O. Silva, V. Costa Bassetto, D. Baster, M. Mensi, E. Oveisi, H.H. Girault, Oxidative print light synthesis thin film deposition of prussian blue, ACS Appl. Electron Mater. 2 (2020) 927–935, https://doi.org/10.1021/acsaelm.9b00854.
[12] A. Kraft, Some considerations on the structure, composition, and properties of prussian blue: a contribution to the current discussion, Ion. (Kiel.) 27 (2021) 2289–2305, https://doi.org/10.1007/s11581-021-04013-0.
[13] M.A. Busquets, J. Estelrich, Prussian blue nanoparticles: synthesis, surface modification, and biomedical applications, Drug Discov. Today 25 (2020) 1431–1443, https://doi.org/10.1016/j.drudis.2020.05.014.
[14] Y. Wang, Z. Liang, Z. Liang, W. Lv, M. Chen, Y. Zhao, Advancements of prussian blue-based nanoplatforms in biomedical fields: progress and perspectives, J. Control. Release 351 (2022) 752–778, https://doi.org/10.1016/j.jconrel.2022.10.007.
[15] Y. Wang, X. Pang, J. Wang, Y. Cheng, Y. Song, Q. Sun, et al., Magnetically-targeted and near infrared fluorescence/magnetic resonance/photoacoustic imaging-guided combinational anti-tumor phototherapy based on polydopamine-capped magnetic Prussian blue nanoparticles, J. Mater. Chem. B 6 (2018) 2460–2473, https://doi.org/10.1039/C8TB00483H.
[16] S. Blasa, M. Borzenkov, V. Pastori, L. Doveri, P. Pallavicini, G. Chirico, et al., prussian blue nanoparticle-mediated scalable thermal stimulation for in vitro neuronal differentiation, nanomaterials 12 (2022) 2304, https://doi.org/10.3390/nano12132304.
[17] A.M. Goodman, O. Neumann, K. Nørregaard, L. Henderson, M.-R. Choi, S.E. Clare, et al., Near-infrared remotely triggered drug-release strategies for cancer treatment, Proc. Natl. Acad. Sci. 114 (2017) 12419–12424, https://doi.org/10.1073/pnas.1713137114.
[18] Z. Wan, P. Zhang, L. Lv, Y. Zhou, NIR light-assisted phototherapies for bone-related diseases and bone tissue regeneration: A systematic review, Theranostics 10 (2020) 11837–11861, https://doi.org/10.7150/thno.49784.
[19] C. Wang, Y. Liu, Y. Zhang, Y. Song, Q. Chen, A. Cai, et al., Synthesis, photothermal effects, and antibacterial properties of lanthanum-doped hydroxyapatite, Ceram. Int 49 (2023) 11378–11392, https://doi.org/10.1016/j.ceramint.2022.11.337.
[20] Y. Lu, L. Li, M. Li, Z. Lin, L. Wang, Y. Zhang, et al., Zero-dimensional carbon dots enhance bone regeneration, osteosarcoma ablation, and clinical bacterial eradication, bioconjug Chem. 29 (2018) 2982–2993, https://doi.org/10.1021/acs.bioconjchem.8b00400.
[21] N.C. Köseoğlu, A. Büyükaksoy, A.Y. Oral, M.H. Aslan, Hydroxyapatite/bioactive glass films produced by a sol–gel method: in vitro behavior, Adv. Eng. Mater. 11 (2009), https://doi.org/10.1002/adem.200900034.
[22] X. Ren, Z. Sun, X. Ma, Y. Wang, X. Cui, Z. Yi, et al., Alginate-mediated mineralization for ultrafine hydroxyapatite hybrid nanoparticles, Langmuir 34 (2018) 6797–6805, https://doi.org/10.1021/acs.langmuir.8b00151.
[23] L. Wang, Y. Li, C. Li, In situ processing and properties of nanostructured hydroxyapatite/alginate composite, J. Nanopart. Res. 11 (2009) 691–699, https://doi.org/10.1007/s11051-008-9431-y.
[24] Y.-H. Liang, C.-H. Liu, S.-H. Liao, Y.-Y. Lin, H.-W. Tang, S.-Y. Liu, et al., Cosynthesis of cargo-loaded hydroxyapatite/alginate core–shell nanoparticles (hap@alg) as ph-responsive nanovehicles by a pre-gel method, ACS Appl. Mater. Interfaces 4 (2012) 6720–6727, https://doi.org/10.1021/am301895u.
[25] G. Liu, B. Li, J. Li, J. Dong, V.E. Baulin, Y. Feng, et al., Photothermal carbon dots chelated hydroxyapatite filler: high photothermal conversion efficiency and enhancing adhesion of hydrogel, ACS Appl. Mater. Interfaces 15 (2023) 55335–55345, https://doi.org/10.1021/acsami.3c11957.
[26] Y.-G. Zhang, Y.-J. Zhu, F. Chen, B.-Q. Lu, Dopamine-modified highly porous hydroxyapatite microtube networks with efficient near-infrared photothermal effect, enhanced protein adsorption and mineralization performance, Colloids Surf. B Biointerfaces 159 (2017) 337–348, https://doi.org/10.1016/j.colsurfb.2017.07.093.
[27] G.S. Correia, J.S.A. Falcão, A.G. Castro Neto, Y.J.A. Silva, L.T.B. Mendonça, A.O. S. Barros, et al., In situ preparation of nanohydroxyapatite/alginate composites as additives to PVA electrospun fibers as new bone graft materials, Mater. Chem. Phys. 282 (2022) 125879, https://doi.org/10.1016/j.matchemphys.2022.125879.
[28] I. Mobasherpour, M.S. Heshajin, A. Kazemzadeh, M. Zakeri, Synthesis of nanocrystalline hydroxyapatite by using precipitation method, J. Alloy. Compd. 430 (2007) 330–333, https://doi.org/10.1016/j.jallcom.2006.05.018.
[29] X. Liu, B. Li, F. Fu, K. Xu, R. Zou, Q. Wang, et al., Facile synthesis of biocompatible cysteine-coated CuS nanoparticles with high photothermal conversion efficiency for cancer therapy, Dalton Trans. 43 (2014) 11709, https://doi.org/10.1039/C4DT00424H.
[30] F.D.C. Gomes, J.D.P. de Amorim, G.S. da Silva, K.C. de Souza, A.F. Pinto, B. S. Santos, et al., Preparation and characterization of hydroxyapatite by the precipitation method and heat treatment, Res., Soc. Dev. 9 (2020) e172963549, https://doi.org/10.33448/rsd-v9i6.3549.
[31] S.-C. Jang, S.-B. Hong, H.-M. Yang, K.-W. Lee, J.-K. Moon, B.-K. Seo, et al., Removal of radioactive cesium using prussian blue magnetic nanoparticles, Nanomaterials 4 (2014) 894–901, https://doi.org/10.3390/nano4040894.
[32] A. Mamaeva, A. Kenzhegulov, A. Panichkin, R. Abdulvaliyev, B. Kshibekova, T. Arynbayev, Mechanical grinding of hydroxyapatite and its interaction with titanium, Coatings 14 (2024) 333, https://doi.org/10.3390/coatings14030333.
[33] A. Sobczak-Kupiec, D. Malina, M. Piatkowski, K. Krupa-Żuczek, Z. Wzorek, B. Tyliszczak, physicochemical and biological properties of hydrogel/gelatin/hydroxyapatite paa/g/hap/agnps composites modified with silver nanoparticles, J. Nanosci. Nanotechnol. 12 (2012) 9302–9311, https://doi.org/10.1166/jnn.2012.6756.
[34] A.M. Farah, C. Billing, C.W. Dikio, A.N. Dibofori-Orji, O.O. Oyedeji, D. Wankasi, et al., Synthesis of prussian blue and its electrochemical detection of hydrogen peroxide based on cetyltrimethylammonium bromide (ctab) modified glassy carbon electrode, Int J. Electrochem Sci. 8 (2013) 12132–12146, https://doi.org/10.1016/S1452-3981(23)13250-0.
[35] M.K. Shahid, J.Y. Kim, Y.-G. Choi, Synthesis of bone char from cattle bones and its application for fluoride removal from the contaminated water, Ground Sustain Dev. 8 (2019) 324–331, https://doi.org/10.1016/j.gsd.2018.12.003.
[36] H. Seema, N. Khan, A. ul H.A. Shah, A. Muhammad, Fabrication of self-assembled Prussian blue graphene hydrogel for highly selective removal of radioactive cesium in water: Adsorption study, Mater. Chem. Phys. 306 (2023), https://doi.org/10.1016/j.matchemphys.2023.128003.
[37] V. Sathiyajothi, N. Viswanathan, M. Naushad, Facile fabrication of hydroxyapatite and bentonite encapsulated biopolymeric hybrid composites for selective removal of methylene blue, ChemistrySelect 9 (2024), https://doi.org/10.1002/slct.202303242.
[38] X. Zhang, Q. Qu, W. Cheng, A. Zhou, Y. Deng, W. Ma, et al., A Prussian blue alginate microparticles platform based on gas-shearing strategy for antitumor and antibacterial therapy, Int J. Biol. Macromol. 209 (2022) 794–800, https://doi.org/10.1016/j.ijbiomac.2022.04.064.
[39] H. Pan, C. Zhang, T. Wang, J. Chen, S.-K. Sun, In Situ Fabrication of intelligent photothermal indocyanine green–alginate hydrogel for localized tumor ablation, ACS Appl. Mater. Interfaces 11 (2019) 2782–2789, https://doi.org/10.1021/acsami.8b16517.
[40] G.S. Correia, J.S.A. Falcão, A.G. Castro Neto, Y.J.A. Silva, L.T.B. Mendonça, A.O. S. Barros, et al., In situ preparation of nanohydroxyapatite/alginate composites as additives to PVA electrospun fibers as new bone graft materials, Mater. Chem. Phys. 282 (2022) 125879, https://doi.org/10.1016/j.matchemphys.2022.125879.
[41] Y.-H. Liang, C.-H. Liu, S.-H. Liao, Y.-Y. Lin, H.-W. Tang, S.-Y. Liu, et al., cosynthesis of cargo-loaded hydroxyapatite/alginate core–shell nanoparticles (HAP@ALG) as ph-responsive nanovehicles by a pre-gel method, ACS Appl. Mater. Interfaces 4 (2012) 6720–6727, https://doi.org/10.1021/am301895u.
[42] G.S. Correia, J.S.A. Falcão, A.G. Castro Neto, Y.J.A. Silva, L.T.B. Mendonça, A.O. S. Barros, et al., In situ preparation of nanohydroxyapatite/alginate composites as additives to PVA electrospun fibers as new bone graft materials, Mater. Chem. Phys. 282 (2022) 125879, https://doi.org/10.1016/j.matchemphys.2022.125879.
[43] X. Ren, Z. Sun, X. Ma, Y. Wang, X. Cui, Z. Yi, et al., Alginate-mediated mineralization for ultrafine hydroxyapatite hybrid nanoparticles, Langmuir 34 (2018) 6797–6805, https://doi.org/10.1021/acs.langmuir.8b00151.
[44] G. Dacarro, A. Taglietti, P. Pallavicini, Prussian blue nanoparticles as a versatile photothermal tool, Molecules 23 (2018) 1414, https://doi.org/10.3390/molecules23061414.
[45] J. Sun, J. Zhang, L. Zhao, S. Wan, B. Wu, C. Ma, et al., Contribution of hydrogen-bond nanoarchitectonics to switchable photothermal-mechanical properties of bioinorganic fibers, CCS Chem. 5 (2023) 1242–1250, https://doi.org/10.31635/ccschem.022.202201946.